Title

Interseismic Ground Deformation and Fault Slip Rates in the Greater San Francisco Bay Area From Two Decades of Space Geodetic Data

Journal

Journal of Geophysical Research: Solid Earth, 123(9)

ISSN

2169-9313

Authors

Xu, Wenbin
Wu, Songbo
Materna, Kathryn
et al.

Publication Date

2018-09-01

DOI

10.1029/2018jb016004

Peer reviewed

Interseismic Ground Deformation and Fault Slip Rates in the Greater San Francisco Bay Area From Two Decades of Space Geodetic Data

Wenbin Xu[1,2], Songbo Wu[1], Kathryn Materna[2], Robert Nadeau[2], Michael Floyd[3], Gareth Funning[4], Estelle Chaussard[5], Christopher W. Johnson[2], Jessica R. Murray[6], Xiaoli Ding[1], and Roland Bürgmann[2]

[1] Department of Land Surveying and Geo-Informatics, The Hong Kong Polytechnic University, Hong Kong, China, [2] Berkeley Seismological Laboratory and Department of Earth and Planetary Science, University of California, Berkeley, CA, USA, [3] Department of Earth, Atmospheric and Planetary Sciences, Massachusetts Institute of Technology, Cambridge, MA, USA, [4] Department of Earth Sciences, University of California, Riverside, CA, USA, [5] Department of Geology, State University of New York, Buffalo, NY, USA, [6] U.S. Geological Survey, Menlo Park, Menlo Park, CA, USA

Correspondence to: W. Xu, wenbin.xu@polyu.edu.hk

Abstract

The detailed spatial variations of strain accumulation and creep on major faults in the northern San Francisco Bay Area (North Bay), which are important for seismic potential and evaluation of natural hazards, remain poorly understood. Here we combine interferometric synthetic aperture radar data from the ERS-1/2 and Envisat satellites between 1992 and 2010 with continuous and campaign GPS data to obtain a high spatial and temporal coverage of ground deformation of the North Bay. The SAR data from both ascending and descending orbits are combined to separate horizontal and vertical components of the deformation. We jointly invert the horizontal component of the mean velocities derived from these data to infer the deep strike-slip rates on major locked faults. We use the estimated deep rates to simulate the long-wavelength deformation due to interseismic elastic strain accumulation along these locked faults. After removing the long-wavelength signal from the InSAR horizontal mean velocity field, we estimate fault-parallel surface creep rates of up to 2 mm/year along the central section of the Rodgers Creek fault and surface creep rates ranging between 2 and 4 mm/year along the Concord fault. No surface creep is geodetically resolved along the West Napa and Green Valley fault zones. We identified characteristically repeating earthquakes on the Rodgers Creek fault, the West Napa fault, the Green Valley fault, and the Concord fault. Nontectonic deformation in the Geysers geothermal field and in Late Cenozoic basins (Rohnert Park and Sonoma basins) are also observed, likely due to hydrological and sediment-compaction processes, respectively.

1 Introduction

The San Andreas Fault System in the northern San Francisco Bay Area (North Bay) consists of four major subparallel strands, the northern San Andreas, Rodgers Creek-Maacama, West Napa, and Concord-Green Valley-Bartlett Springs fault zones (Figure 1). Several moderate to large earthquakes have

occurred on these faults during the past century. In 1906, a M_w 7.8 earthquake took place on the northern San Andreas fault with a total rupture length of ~470 km (Thatcher et al., 1997) causing significant damage to the city of San Francisco. In 1969, two damaging moderate magnitude (M_L 5.6 and M_L 5.7) earthquakes occurred near the city of Santa Rosa, likely on the Healdsburg section of the Rodgers Creek fault (Wong & Bott, 1995). More recently, a M_w 6 earthquake ruptured the West Napa fault on 24 August 2014, causing significant economic damage in the region (e.g., Earthquake Engineering Research Institute, 2015). No major earthquakes have occurred during the historical record on either the Maacama fault, the Concord-Green Valley fault, or the Bartlett Springs fault, despite the accumulation of a slip deficit that is now likely large enough to generate M_w ~7 earthquakes on these faults (Freymueller et al., 1999; Murray et al., 2014). Compared to the well-studied faults in the central Bay Area (Bürgmann et al., 2000; Chaussard, Bürgmann, Fattahi, Johnson, et al., 2015; d'Alessio et al., 2005; Shirzaei & Bürgmann, 2013), the spatial variations of strain accumulation and creep on major faults in the North Bay remain poorly understood.

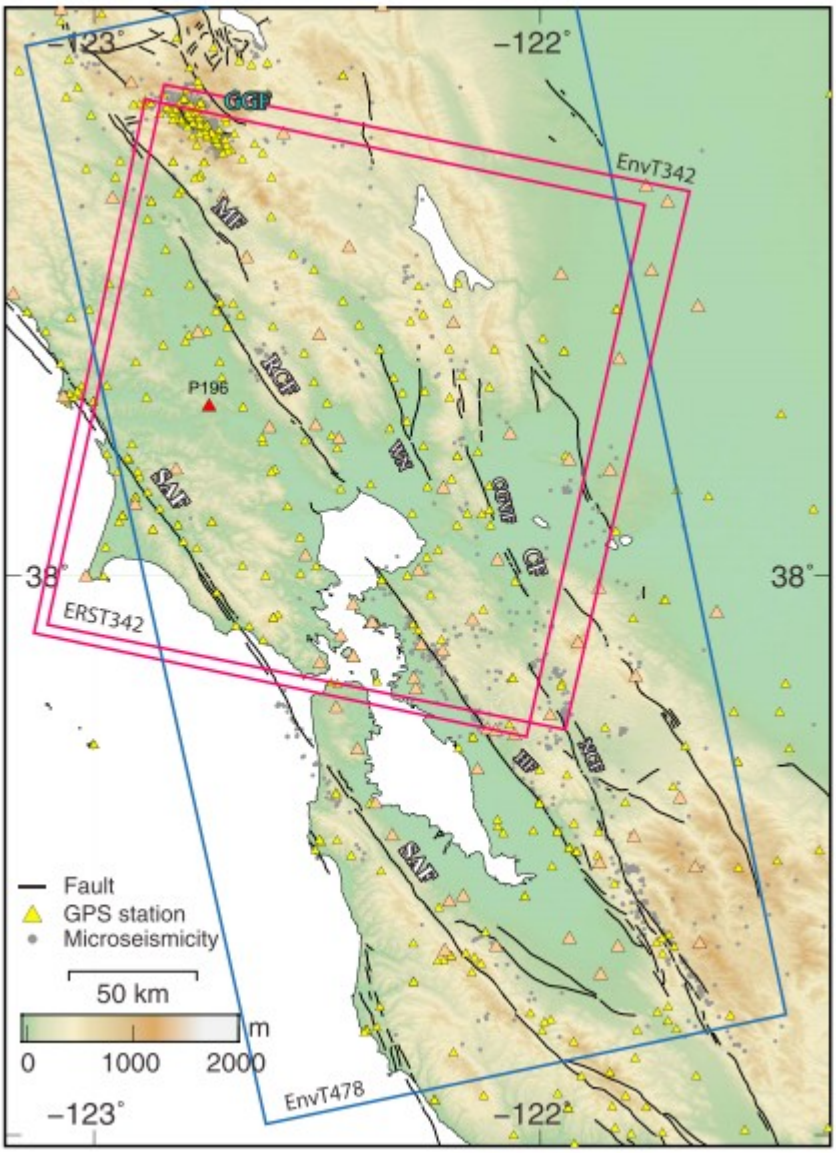

Figure 1

Map showing the data sets used in the study. The red and blue rectangles outline the existing InSAR scenes with tracks and satellite noted. The triangles indicate the location of continuous GPS sites (pink) from the PBO and BARD GPS networks and North Bay campaign sites (yellow). The reference GPS station P196 is highlighted in red. Active faults in the studied area shown in black lines: SAF, San Andreas fault; RCF, Rogers Creek fault; MF, Maacama fault; WN, West Napa fault; CGVF: Concord-Green Valley fault; CF, Concord fault; HF, Hayward fault; NCF, Northern Calaveras fault; GGF, Geysers geothermal field.

Interseismic deformation and fault creep have been primarily estimated from Global Positioning System (GPS) and alignment array (AA) data in the North Bay. Freymueller et al. (1999) simultaneously estimated the locking depths and deep slip rates of the northern San Andreas fault, Maacama fault, and Bartlett Springs fault using 2-D models. They found deep slip rates of $17.4^{+2.5}_{-3.1}$ mm/year, $13.9^{+4.1}_{-2.8}$ mm/year, and $8.2^{+2.1}_{-1.9}$ mm/year and locking depths of $14.9^{+12.5}_{-7.1}$

km, $13.4^{+7.4}_{-4.8}$ km, and 0 km for the northern San Andreas fault, Maacama fault, and Bartlett Springs fault, respectively. Based on the analysis of both campaign and continuous GPS data collected between 1992 and 2000, Prescott et al. (2001) estimated a 20.8 ± 1.9 mm/year deep slip rate on the northern San Andreas fault, 10.3 ± 2.6 mm/year on the Rodgers Creek fault, and 8.1 ± 2.1 mm/year on the Concord-Green Valley fault, respectively. The estimated locking depths are 11, 12, and 14 km for the northern San Andreas fault, Rodgers Creek fault, and Green Valley fault, respectively. Prescott et al. (2001) found a slightly higher slip rate for the Green Valley fault than that estimated from geologic data, and the inferred slip rate for the SAF is somewhat lower than the geologic rate (Niemi & Hall, 1992). Murray et al. (2014) estimated the deep slip rates on the northern San Andreas fault, Maacama fault, and Bartlett Springs fault to be 21.5 ± 0.5, 13.1 ± 0.8, and 7.5 ± 0.7 mm/year below 16, 9, and 13 km, respectively, using an expanded campaign GPS network spanning a latitude range between 39° and 40°. AAs and GPS suggest that the northern San Andreas fault is fully locked and the other major faults are partially creeping at variable rates (Galehouse & Lienkaemper, 2003; Lienkaemper et al., 2014; Murray et al., 2014). However, the limited spatial coverage of the ground-based geodetic data does not allow a complete recording of the near-field interseismic deformation associated with these faults and therefore prohibits a more refined assessment of their earthquake potential.

Interferometric synthetic aperture radar (InSAR) has been widely used to constrain the locations of actively creeping faults in areas with limited ground access (Jolivet et al., 2012; Metzger & Jónsson, 2014; Ryder & Bürgmann, 2008). It has provided important information on the spatio-temporal distribution of shallow aseismic fault slip (Çakir et al., 2005; Fattahi & Amelung, 2016). The combination of InSAR and GPS data has led to refined estimates of the amplitude of elastic strain accumulation on seismogenic faults and their locking depths with both a high spatial and temporal coverage (Tong et al., 2013; Wright et al., 2001). Where large data sets are available InSAR has shown its ability to characterize both the long- and short-wavelength deformation to a very high accuracy, independent of GPS data (e.g., Chaussard, Bürgmann, Fattahi, Johnson, et al., 2015). A 30-image ERS satellite-based Permanent Scatterer InSAR (PS-InSAR) study spanning the time interval 1992–2001 suggests that the Rodgers Creek fault is undergoing as much as 7.5 ± 2.6 mm/year of shallow creep above a depth of ~6 km (Funning et al., 2007). Combining Envisat data from both ascending and descending orbits, Jin and Funning (2017) found evidence for surface creep along a 20-km-long segment of the Rodgers Creek fault with rates between 1.9 and 6.7 mm/year.

In this work, we expand previous studies by using a more complete InSAR data set covering the major faults in both ascending and descending orbits and spanning an ~20-year time window between 1992 and 2010. We align the InSAR data to GPS velocities and deconvolve the InSAR mean velocities

into horizontal and vertical components. We combine our new results from the North Bay with InSAR and updated GPS data from the central Bay Area (Chaussard, Bürgmann, Fattahi, Nadeau, et al., 2015). We invert for the deep strike-slip rates on major faults in the greater Bay Area and use a forward model to simulate and remove the long wavelength signal from the fault horizontal mean velocity field. The remaining short-wavelength deformation shows that shallow creep occurs along the Rodgers Creek and Concord faults; however, the data are not of high enough quality to allow for inversion of meaningful distributed creep models. We also observe significant and localized nontectonic surface processes in the North Bay.

2 Data and Methods

2.1 InSAR Data Processing and Time Series Analysis

In this study, data from three different satellites (i.e., ERS-1/2 and Envisat with a total of 88 SAR images) are used to resolve the 1992–2010 interseismic deformation in the North Bay. These data from two tracks (descending track 342 and ascending track 478) were obtained from the European Space Agency (ESA) through the Western North American interferometric synthetic aperture radar consortium (WInSAR) archive (Figure 1). After the concatenation of adjacent frame data sets, 274 interferograms were generated (Figure S1 and Table S1). In the interferometric chain, the 1 arc/sec (~30 m) Shuttle Radar Topography Mission digital elevation model (Farr et al., 2007) is utilized to simulate and eliminate the topographic phase contribution with the GAMMA software. To increase the signal-to-noise ratio, the interferograms are multilooked to around 100 square meters per pixel. We use the amplitude dispersive index of 0.6 (Ferretti et al., 2001) to identify the candidate stable points. These selected points are spatially networked with arcs (e.g., triangular network or fully connected network) with each arc representing the double phase difference between two points. We unwrap the arcs temporally following the temporarily coherent point method presented by Pepe and Lanari (2006) and Fornaro et al. (2011). The advantage of this unwrapping method is that it considers the phase triangularity algorithm in the SAR temporal/perpendicular baseline domain (Ferretti et al., 2011; Monti-Guarnieri & Tebaldini, 2008; Rocca, 2007). We estimate the phase interval vector $\Delta\varphi_i^{\text{arc}}$ on each arc using the least squares inversion method. The detailed estimation of the double phase difference on the *i*th arc is shown as follows:

$$\underbrace{\mathbf{A}}_{M\times(N-1)} * \underbrace{\Delta\boldsymbol{\varphi}_{\mathbf{i}}^{\mathbf{arc}}}_{(N-1)\times 1} + \mathbf{e_i} = \underbrace{\Delta\boldsymbol{\Phi}_{\mathbf{i}}^{\mathbf{arc}}}_{M\times 1}$$

$$\mathbf{A}=\begin{bmatrix} 1 & 1 & 0 & 0 & \cdots \\ 0 & 1 & 1 & 1 & \cdots \\ \cdots & \cdots & \cdots & \cdots & \cdots \\ \cdots & \cdots & \cdots & \cdots & \cdots \end{bmatrix}$$

$$\Delta\boldsymbol{\varphi}_{\mathbf{i}}^{\mathbf{arc}}(\boldsymbol{\theta}) = (\boldsymbol{\theta}_1\boldsymbol{\theta}_2\cdots\boldsymbol{\theta}_{N-1})^{\mathbf{T}} \quad (1)$$

where **A** represents the matrix with the dimensions of M by N − 1 (M is the number of interferograms, N is the number of SAR images). More specifically, if the *m*th interferogram covers *n* consequent time intervals, then the corner (*m*, *n*) of **A** is equal to one and contains zeros elsewhere. The $\mathbf{e_i}$ represents the estimated data errors. The $\Delta\boldsymbol{\varphi}_{\mathbf{i}}^{\mathbf{arc}}$ is the N − 1 by 1 matrix collecting the phase interval vector on the arc, $\boldsymbol{\theta}_{\mathbf{i}}$ is the double difference phase on the arc, and $\Delta\boldsymbol{\Phi}_{\mathbf{i}}^{\mathbf{arc}}$ represents the double phase difference value on the arc.

Because multilooked interferograms produce phase inconsistencies in the temporal/perpendicular baseline domain (De Zan et al., 2015), we iteratively estimate the phase vector via equation 1 and use the standard deviation of the residual (i.e., σ_{residual} = 0.2 rad) to exclude noisy arcs and weight the calculation in equation 1 (Zhang et al., 2011). Before the integration in the spatial domain, we detect the closure triangles with the remaining arcs and ensure that the residual phase of closure triangularity is close to zero (Agram & Simons, 2015; Hanssen, 2001; Rocca, 2007). The arcs and isolated points that have large phase variations or phase ambiguities are removed (Pepe & Lanari, 2006). Then, the standard deviation of the residual (i.e., σ_{residual}) can reasonably be used to set the weights associated with the single arcs (see (2) $\mathbf{W_p}$). Using equation 2, the spatial integration for spatial phase unwrapping is executed to get unwrapped phase on the points, which is related to a GPS reference station P196 (Figure 1), which is shown as follows:

$$\left(\underbrace{B^{\mathsf{T}}}_{Q\times P}\underbrace{W_{\mathrm{p}}}_{Q\times Q}\underbrace{B}_{Q\times P}\right)\underbrace{\Phi^{\mathbf{point}}}_{P\times N-1} = \underbrace{\mathbf{B}^{\mathbf{T}}}_{Q\times P}\underbrace{\mathbf{W}_{\mathrm{p}}}_{Q\times Q}\underbrace{\Delta\boldsymbol{\varphi}^{\mathbf{arc}}}_{Q\times N-1}$$

$$\mathbf{B} = \begin{bmatrix} 1 & -1 & 0 & 0 & \cdots \\ 0 & 1 & 0 & -1 & \cdots \\ \cdots & \cdots & \cdots & \cdots & \cdots \\ \cdots & \cdots & \cdots & \cdots & \cdots \end{bmatrix}$$

$$\mathbf{W}_{\mathrm{p}} = \begin{cases} \dfrac{1}{(1+\sigma_{\text{residual}})}, & \sigma_{\text{residual}} < \delta \\ 0, & \sigma_{\text{residual}} \geq \delta \end{cases} \quad (2)$$

where $\mathbf{B}$ is a Q by P matrix (Q is the number of arcs and P is the number of points) that presents the network design matrix. The $\Delta\boldsymbol{\varphi}$ collects all the phase vectors on the arc with Q by $N-1$ dimension. $\mathbf{W_p}$ is a Q by Q diagonal weighting matrix and δ is an experimental threshold value. The $\boldsymbol{\phi}^{\mathbf{point}}$ is a P by $N-1$ matrix containing the phase history vector on the points.

When the unwrapped phase history vectors of the points are available, the deformation and topographic residual can be parameterized and estimated. Noise from atmospheric artifacts is reduced using a principal component analysis-based inversion method (Lin et al., 2010). In addition, the Local Oscillator Drift (LOD) seen in the Envisat interferograms is corrected using the empirical model proposed by Marinkovic and Larsen (2013). The remaining data noise mainly consists of small orbital errors and atmospheric artifacts, which we mitigate with the help of all available 3-D GPS velocities. We identify the noisy part from the InSAR long wavelength deformation field and use the GPS to constrain a quadratic function.

After we remove the estimated ramps from the LOS velocity maps on the different tracks; that is, ascending and descending orbits, we assume that the updated LOS velocity is a combination of the east-west horizontal displacement rate (u_e) and vertical motion (u_v). Because InSAR is least sensitive to north-south motion because of its near polar orbits, we ignore this component of the displacement (Fialko et al., 2001). We validate the decomposed velocity fields by comparing them with GPS east-west and vertical velocities and observe agreement with an RMS value of ~3 and ~9 mm/year, respectively (Figure S2). Note that the RMS decreases to 2 and 4 mm/year if the Geysers region is excluded. This is likely due to deformation rates associated with the geothermal extraction and injection activity at the Geysers varying strongly in time (Floyd & Funning, 2013; Mossop & Segall, 1997; Vasco et al., 2013).

2.2 GPS Data Processing

For comparison with the InSAR-derived velocity field, we compile multiple sources of GPS velocities into a single GPS velocity field. This reference velocity field includes the Bay Area Velocity Unification model (BAVU4) velocity field, derived from campaign GPS measurements in the Bay Area and processed with the GAMIT/GLOBK software (Herring et al., 2010a). This represents an update of the GPS velocities presented by d'Alessio et al. (2005) with more recently collected data in the central Bay Area. Velocities from the Plate Boundary Observatory and Bay Area Regional Deformation network are combined with BAVU4 using the GLOBK software package (Herring et al., 2010b). In addition, velocity fields from the United States Geological Survey (USGS) campaign and continuous networks (Murray & Svarc, 2017) and from Floyd et al. (2016) are also combined into the reference field. Time series are fit with a linear trend and seasonal (annual plus semiannual) terms for time series longer than two years, as well as any significant discontinuities due to equipment changes and earthquakes. To

estimate the effect of temporal correlations in the data, the normalized root-mean-squared (RMS) misfit to this fit is calculated over different intervals and extrapolated using an exponential function, based on a first-order Gauss-Markov process, to the asymptote at infinite time series length to calculate a scaling factor for the formal uncertainty (e.g., Herring, 2003; Reilinger et al., 2006). These scaled velocity uncertainties are converted to an equivalent magnitude of random walk noise based on the length of the time series (e.g., Zhang et al., 1997), which is then incorporated into GLOBK's Kalman filter to account for temporal correlations during final combination of daily results to estimate velocities. For the velocity field combinations, we used a six-parameter Helmert transformation with three rotation and three translation parameters to minimize the misfit between the stations common to multiple networks. We exclude 144 out of 1592 stations with formal uncertainties of more than 3 mm/year from the Helmert transformation and combined velocity field. The resulting velocity field represents a dense collection of Bay Area campaign and continuous GPS velocities with respect to a common reference. The RMS misfit values during the adjustment of velocity fields by Helmert transformation ranged from 0.7 to 1.7 mm/year for the common stations.

2.3 Repeating Earthquakes

While geodetic data provide information on fault slip at depth through the filter of the Earth's crust, characteristically repeating earthquakes (CREs) provide direct measurements of creep at their precise location at depth on an actively creeping fault plane (Chaussard, Bürgmann, Fattahi, Nadeau, et al., 2015; Nadeau & McEvilly, 1999; Nadeau & McEvilly, 2004). Considering the uncertainty of the method, CREs may represent creep slip events such that creep rates derived from CRE recurrence times would represent minimum bounds (Beeler et al., 2001). CRE sequences are events occurring in essentially identical locations, with similar magnitudes, and with high waveform correlation coefficients. We searched for the existence of CREs on the North Bay faults to identify creeping fault sections. We used the Double-Difference Real-Time catalog and follow the method of Turner et al. (2013) relying on events from the Northern California Earthquake Data Center (NCEDC) detected by the Northern California Seismic System (NCSS). We have developed an automated method of waveform cross-correlation analysis in the frequency domain using an ~5-s data window starting ~0.5 s before the *P* wave phase arrival performed on pairs of events with >M 1.2 and hypocentral separations ≦10 km. We consider potential CRE event pairs with maximum cross-correlation values >0.6, focusing on event identification rather than on the full characterization of CRE sequences. We find four repeating sequences on the Rodgers Creek fault, two of which are located to the south of Santa Rosa at ~4.5 km depth with a magnitude <3, the other two found north of Santa Rosa at depths of 6.5 km and 9.1 km with a magnitude of ~2, respectively. Two CREs of magnitudes <2 are found on the Concord fault at a depth of ~6 km. There are two sequences near the West

Napa fault with a magnitude of 1.8 at depths of 6.5 and 7.3 km, respectively. Three CREs with magnitudes ranging between 1.8 and 2.5 are aligned with the Concord Green Valley fault zone at depths increasing from 2.7 km in south to 8 km in north. In contrast, a substantially larger number of CREs are identified on the partially coupled Hayward and Calaveras faults that creep at rates of up to 14 mm/year (Chaussard, Bürgmann, Fattahi, Nadeau, et al., 2015).

3 Surface Creep in the North Bay

The descending ERS-1/2 data comprise SAR images obtained between April 1992 and July 2002 (Figure 2 and Table S1) and show surface creep along the Concord fault and sections of the Rodgers Creek fault. The creeping signal generated by the Hayward fault is also clear. It is difficult to resolve whether surface creep occurs on other major faults in the North Bay from this single viewing geometry. The descending Envisat data (Figure 3), covering a later and shorter time period (2006–2010), confirms the observations of the ERS-1/2 data. The viewing geometry of the ascending Envisat mean velocity field, however, is less favorably oriented to resolve horizontal motion along the San Andreas fault system (Figure 4). Therefore, the ground deformation seen from the ascending data more likely reflects vertical motions.

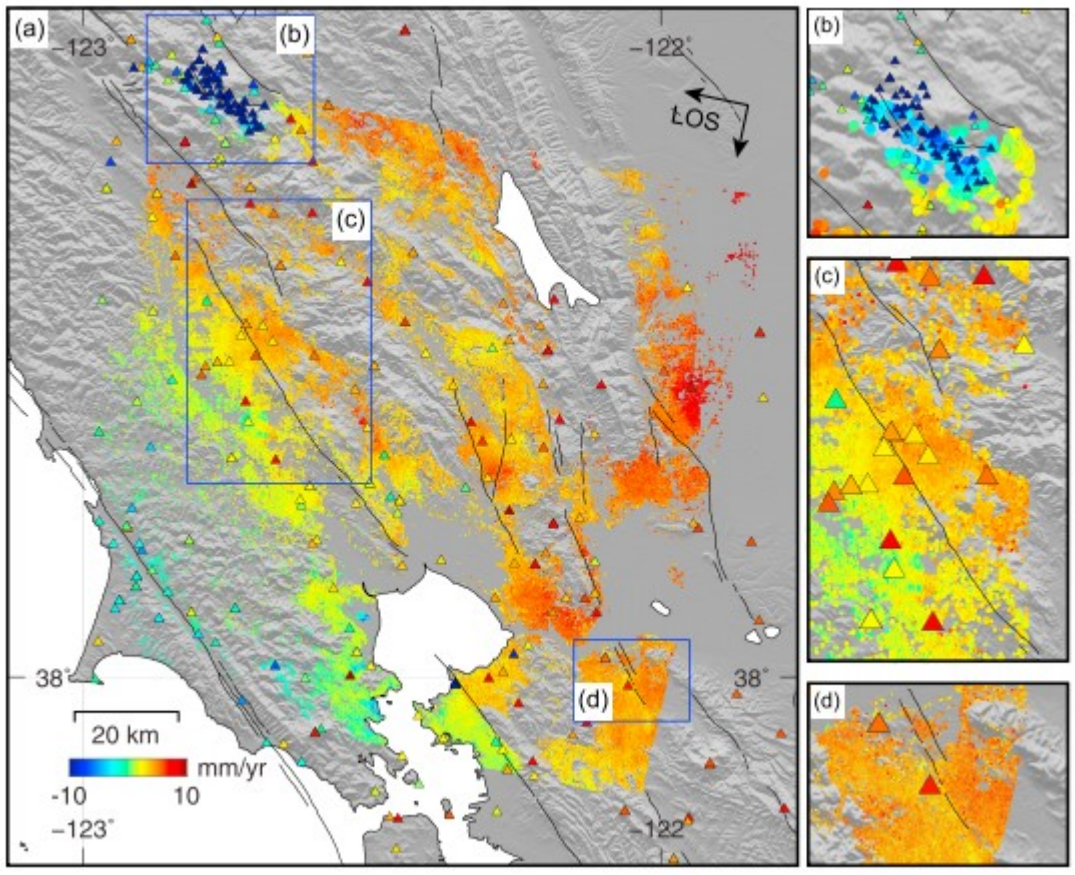

Figure 2

(a) InSAR mean LOS velocity field and GPS horizontal velocities projected into LOS (color-coded triangles) covering the major faults in the North Bay generated using ERS-1/2 SAR data (between April 1992 and July 2002) from the descending orbit. The solid black lines represent the mapped fault traces. Negative LOS values indicate the ground moves away from the satellite. (b–d) Enlarged view of the Geysers geothermal region, the RCF and the CF. Note that the color scale is the same in different subpanels.

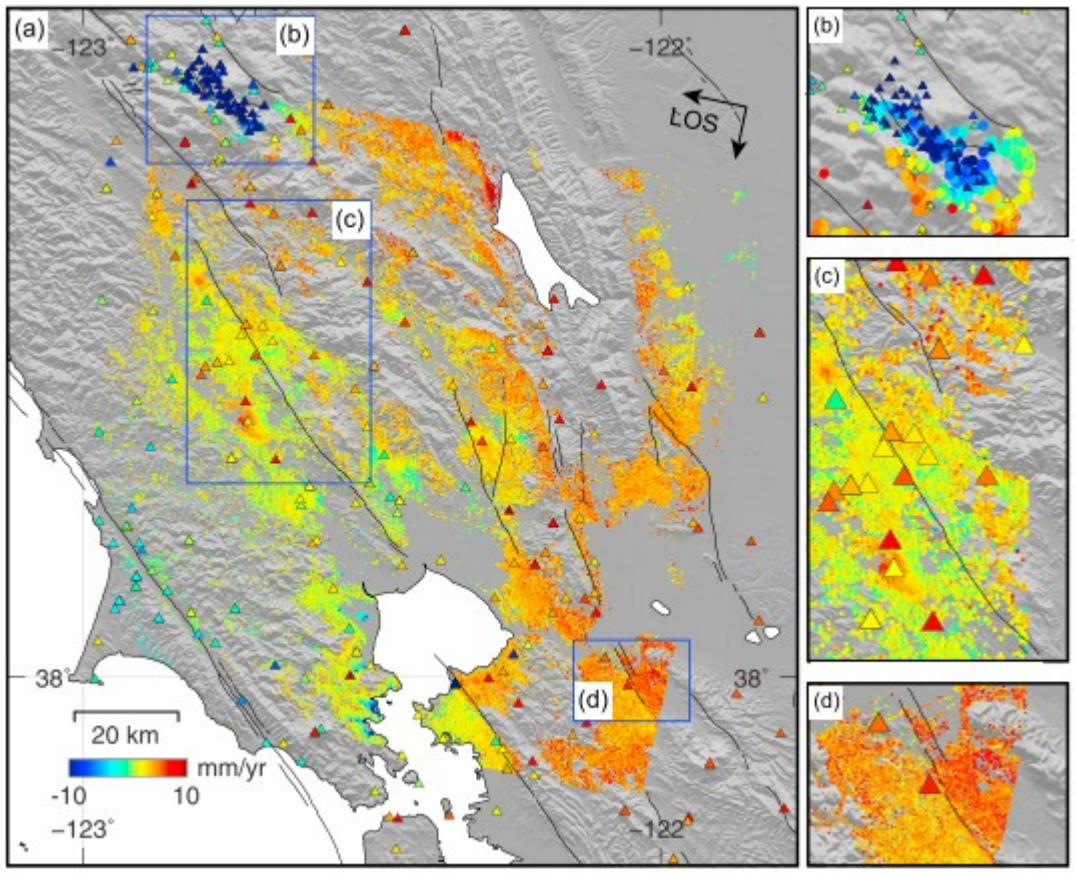

Figure 3

Same as Figure 2 but for the descending Envisat SAR data spanning May 2006 through October 2010.

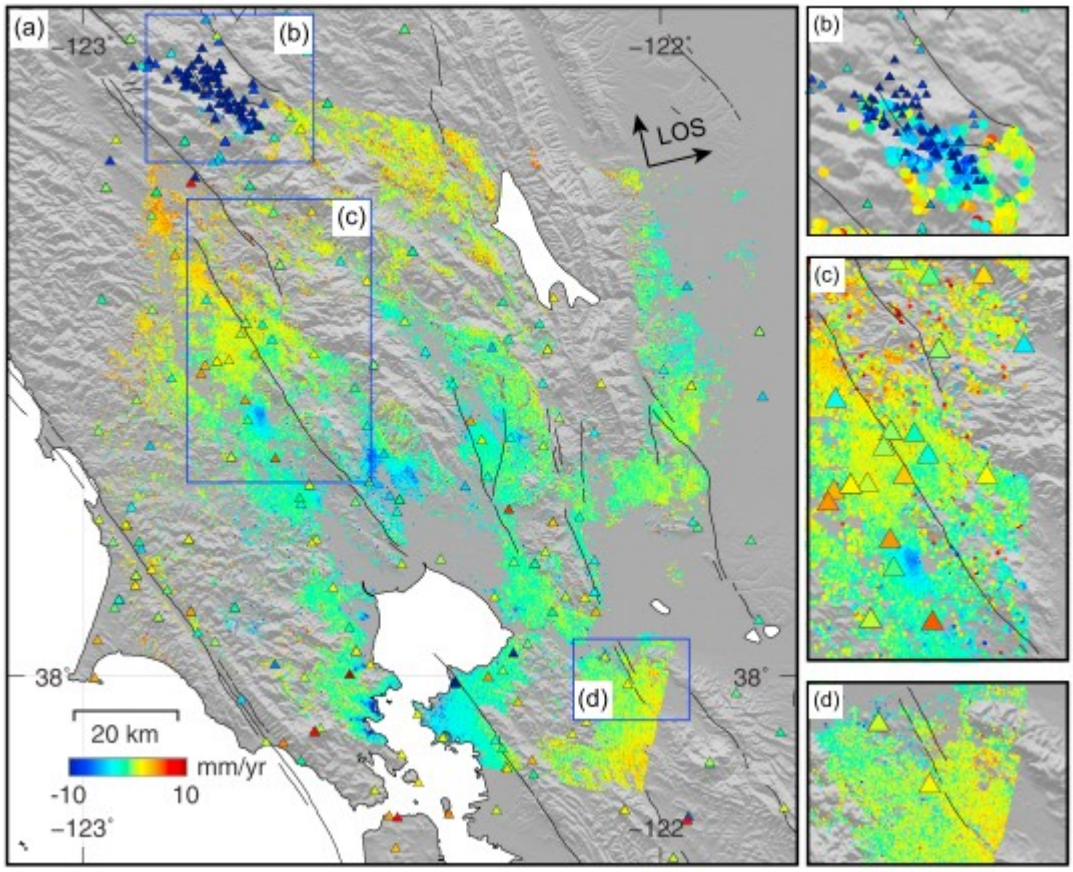

Figure 4

Same as Figure 2, but for the ascending Envisat SAR data spanning October 2006 through October 2010.

Through the decomposition of the ascending and descending InSAR mean velocity fields, we resolve a detailed spatial coverage of the interseismic InSAR mean horizontal velocity and vertical motions in the North Bay where the descending and ascending images overlap. The horizontal deformation includes two main components: the long-wavelength deformation resulting from interseismic elastic strain accumulation along locked faults in the Bay Area (Figure 5a) and the short-wavelength deformation seen near the Rodgers Creek, Concord, and Hayward-Calaveras faults, representing shallow creep (Figure 6). We adopt the Bay Area fault geometry of Funning et al. (2007) and combine our data with the published central Bay Area data (Chaussard, Bürgmann, Fattahi, Nadeau, et al., 2015) to cover major faults in the greater Bay Area. To model the data, we use the rectangular dislocation model (Okada, 1985) assuming a homogeneous and isotropic elastic half-space. We mask out near-fault (<1 km) data from the InSAR east mean velocity field and jointly invert both the combined GPS and the InSAR east mean velocity fields to estimate the deep slip rates on major locked faults in the greater Bay Area (Figure 5). The locking depths are adopted from the published result (Funning et al., 2007). The inversion is done using a constrained linear least squares method, in which the slip rates of the faults

that are located outside the study area are fixed. The combined InSAR horizontal mean velocity field and GPS data are equally weighted in the modeling. The simulated long-wavelength deformation (Figure 5b) agrees well with the data with a RMS misfit of ~2.6 mm/year. We find that the reestimated deep slip rates are generally consistent with previous estimates (Bürgmann et al., 2006; Field et al., 2015; Freymueller et al., 1999; Funning et al., 2007; Murray et al., 2014; Prescott et al., 2001). The jointly modeled long-term slip rates are 19.2 ± 0.8 mm/year on the San Andreas Peninsula segment, ~11.6 ± 0.5 mm/year on the Rodgers Creek fault, and ~11.5 ± 0.6 on the Green Valley fault (Table 1).

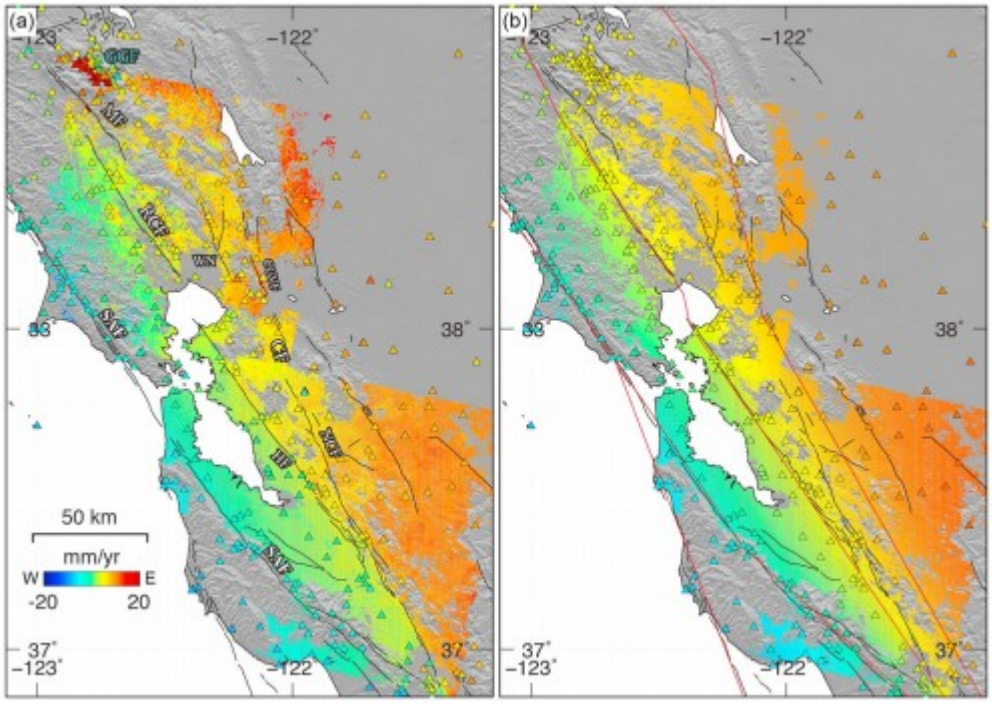

Figure 5

(a) East component of InSAR and GPS mean velocities (color-coded) covering the North Bay (this study) and the central San Francisco Bay Area (from Chaussard, Bürgmann, Fattahi, Johnson, et al., 2015). The colored triangles in (a) show GPS measured east-component velocities of campaign measurements and continuous PBO and BARD stations in the area. Positive values indicate movement to the east in (a). (b) East velocities predicted from the deep dislocation model; the surface trace of the modeled fault geometry is based on Funning et al. (2007). The black lines show the surface projection of the mapped faults. The red lines indicate the surface projection of the vertical dislocations.

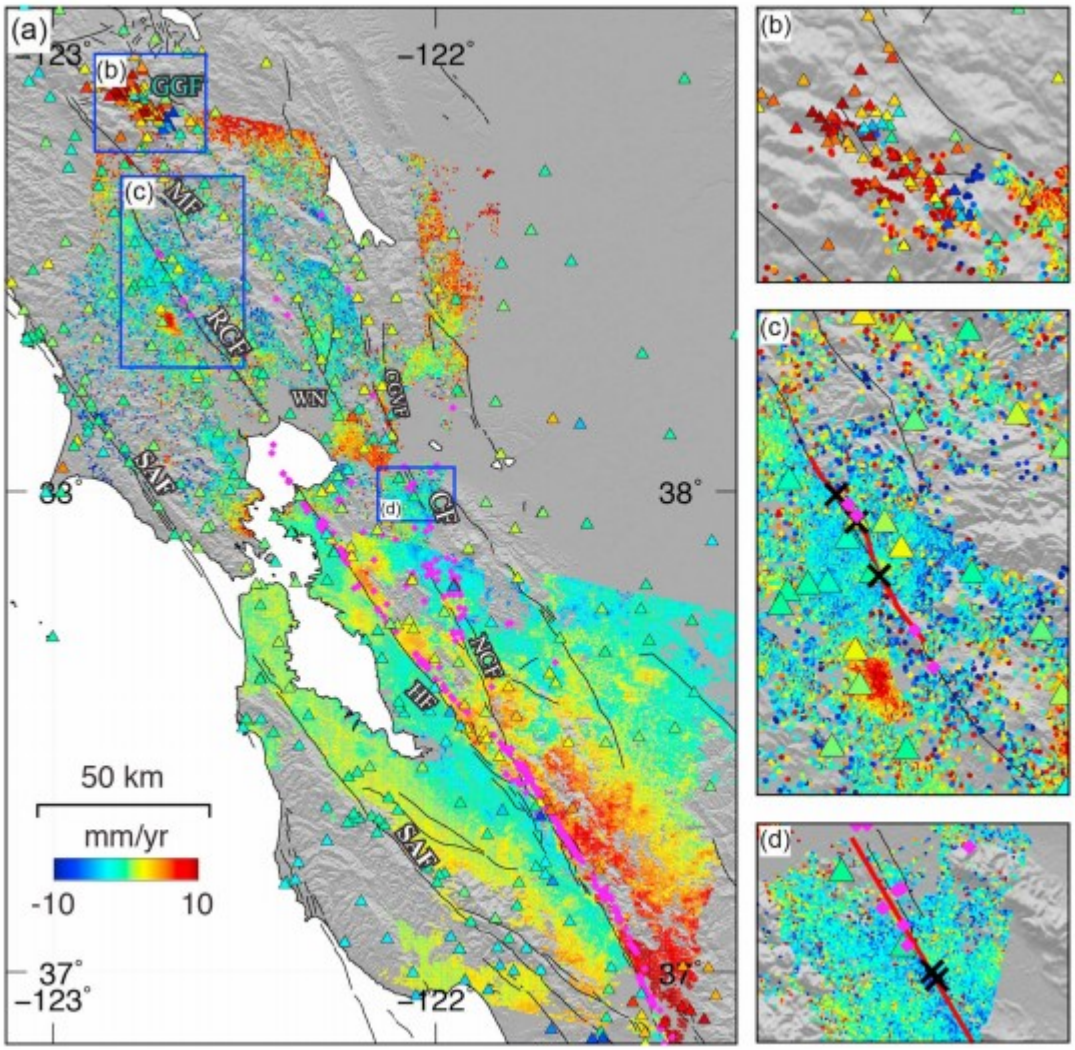

Figure 6

(a) SAF fault-system-parallel (N32°W) residual velocity field of the greater Bay Area obtained by subtracting the long-wavelength deformation from the deep dislocation model shown in Figure 5b. The magenta dots represent the location of repeating earthquakes. (b) Enlarged view of the Geysers geothermal region showing significant horizontal motion. (c) Enlarged view of the RCF-MF. The black crosses indicate the locations of alignment arrays; the red lines indicate the locations of profiles shown in Figure 7. (d) Enlarged view of the concord fault.

Table 1
The Inverted Strike-Slip Rates Based on the Deep Dislocation Model Geometry (Funning et al., 2007) and the Comparison With Existing Geological and Geodetic Rates

	Fault segment						This study			
			SE end		NW end		GPS		InSAR	
Fault name	Top (km)	Bottom (km)	(N)	(E)	(N)	(E)	Slip (mm/year)	Error (+/−)	Slip (mm/year)	Error (+/−)
SanGregorioDeepNorth	13	3000	36.501	−122	37.905	−122.673	2.4	\	2.4	\
SanGregorioDeepSouth	13	3000	35.75	−121.375	36.501	−122	2.4	\	2.4	\
SanGregorioDeepExtendedSouth	14	3000	22.70205	−108.819	35.75	−121.375	2.4	\	2.4	\
GreenValleyDeepExtendedNorth	11	3000	39.97667	−123.4598	55.2659	−137.5289	10.3	\	10.3	\
GreenValleyDeepNorth	11	3000	38.79166	−122.2942	39.9767	−123.4598	10.3	\	10.3	\
GreenValleyDeepSouth	**11**	**3000**	**38.04459**	**−122.0945**	**38.7917**	**−122.2942**	**11.7**	**1**	**11.6**	**1.3**
ConcordDeep	**16**	**3000**	**36.34213**	**−120.8702**	**38.0446**	**−122.0945**	**15.4**	**1.2**	**18.5**	**1**
ConcordDeepExtendedSouth	16	3000	21.11845	−110.1307	36.3421	−120.8702	13.1	\	13.1	\
MaacamaDeepNorth	10	3000	39.83499	−123.6402	55.1011	−137.7137	13.8	\	13.8	\
MaacamaDeepSouth	10	3000	38.66929	−122.8995	39.835	−123.6402	13.8	\	13.8	\
RogersCreekDeep	**10**	**3000**	**38.10899**	**−122.4036**	**38.6693**	**−122.8995**	**7.1**	**1**	**14.8**	**0.6**
RogersCreekHaywardStepoverDeep	10	3000	38.01238	−122.3779	38.109	−122.4036	2.8	\	2.8	\
HaywardDeep	**10**	**3000**	**36.38943**	**−120.9868**	**38.0124**	**−122.3779**	**13.1**	**0.9**	**3.9**	**0.7**
HaywardDeepExtendedSouth	12	3000	21.17035	−110.2261	36.3894	−120.9868	8.9	\	8.9	\
SanAndreasDeepExtendedNorth	15	3000	40.264	−124.241	52.85	−138.83	18.4	\	18.4	\
SanAndreasDeepNorth	15	3000	38.999	−123.69	40.264	−124.241	18.4	\	18.4	\
SanAndreasDeepMarin	**15**	**3000**	**37.905**	**−122.673**	**38.999**	**−123.69**	**17.8**	**0.9**	**18**	**1.7**
SanAndreasDeepPeninsula	**12**	**3000**	**37.324**	**−122.174**	**37.905**	**−122.673**	**19.3**	**1.1**	**20.1**	**1.7**
SanAndreasDeepSouthBay	**14**	**3000**	**36.679**	**−121.286**	**37.324**	**−122.174**	**18.5**	**1.4**	**16.3**	**2.3**
SanAndreasDeepCreepingSegment	15	3000	35.814	−120.359	36.679	−121.286	7.6	\	7.6	\
SanAndreasDeepExtendedSouth	15	3000	22.76599	−107.803	35.814	−120.359	7.6	\	7.6	\

Note. The unbold values are fixed values in the modeling.

Table 1 *(continued)*

		The existing geodetic rates						UCERF3 rate	
InSAR + GPS		Bürgmann et al. (2006)		Funning et al. (2007)		d'Alessio et al. (2005)		Field et al. (2015)	
Slip (mm/year)	Error (+/−)	Slip (mm/year)	Error (+/−)	Slip (mm/year)	Error (+/−)	Slip (mm/year)	Error (+/−)	Slip (mm/year)	Bounds (+/−)
2.4	\	3.5	0.9	2.4	1	2.4	1	7	4–10
2.4	\	\	\	\	\	3	0.8	3	1–7
2.4	\	\	\	\	\	\	\	\	\
10.3	\	\	\	10.3	1.2	\	\	\	\
10.3	\	\	\	10.3	1.2	\	\	\	\
11.5	**0.6**	**20.6**	**0.9**	**10.3**	**1.2**	**7**	**1.8**	**4**	**2–9**
15.9	**0.8**	**20.6**	**0.9**	**13.1**	**2.3**	**4**	**3**	**4.3**	**3–9**
13.1	\	\	\	13.1	2.3	\	\	\	\
13.8	\	\	\	\	\	\	\	\	\
13.8	\	\	\	\	\	\	\	9	6–12
11.6	**0.5**	\	\	**13.8**	**2.3**	**6.6**	**2.4**	**9**	**6–11**
2.8	\	\	\	2.8	34.5	\	\	\	\
9.4	**0.6**	**5.9**	**2.3**	**8.9**	**2.6**	**6.5**	**1.4**	**9**	**7–11**
8.9	\	\	\	\	\	\	\	\	\
18.4	\	\	\	\	\	\	\	\	\
18.4	\	\	\	18.4	2.3	\	\	\	\
18.1	**0.6**	**21.5**	**1.5**	****	****	**20.2**	**1.4**	**24**	**16–27**
19.2	**0.8**	**19.5**	**1**	**18.2**	**1.7**	**17.1**	**1.4**	**17**	**13–21**
19.3	**1.1**	**19.5**	**1**	\	\	**16.4**	**1**	**17**	**13–21**
7.6	\	\	\	\	\	\	\	34	29–39
7.6	\	\	\	\	\	\	\	34	29–39

The short-wavelength deformation is obtained by subtracting the modeled long-wavelength rate (Figure 5b) from the observation (Figure 5a). According to d'Alessio et al. (2005), the total relative motion accommodated by Bay Area faults is 37.9 ± 0.6 mm/year oriented at N30.4°W in the central North Bay and at N34.2°W in the central South Bay. We project the short-wavelength horizontal velocity field into fault-parallel rates in the direction of

N32°W to reflect the actual creep rates. Shallow fault creep is seen along the Hayward and Calaveras faults in the East San Francisco Bay Area (Chaussard, Bürgmann, Fattahi, Nadeau, et al., 2015), while the creep signal is less obvious in the North Bay. We calculate the creep rates based on the difference in fault-parallel velocity binned in boxes on opposite sides of the fault (Figures S3 and S4). Plotting along-fault profiles on our InSAR horizontal velocity map (Figure 7a), we estimate that the average creep rate of the Rodgers Creek fault is about 2 mm/year along much of its trace, consistent with the AA data, although the AA data seem to suggest that the along-fault creep rates decrease from north to south (Figures 7a and S5). Our estimated shallow fault slip rate of 2 mm/year is slightly higher than the lower bound (0.4 mm/year) of a recent estimated value by Jin and Funning (2017) and is much lower than the 6 ± 0.6 mm/year rate that was estimated from seven years of ERS-1/2 data (Funning et al., 2007). Limited near-fault coverage southeast of Santa Rosa prohibits identifying evidence of shallow creep, similar to previous studies (Funning et al., 2007; Jin & Funning, 2017). Another interseismic creep signal ranging between 2 and 4 mm/year is identified along the Concord fault (Figure 7b). These values agree well with the two AA estimates. The InSAR data show that the along-fault creep rate on the northern and southern sections of the Concord fault is likely lower than along its central part (Figure 7b). Similar to previous findings (Chaussard, Bürgmann, Fattahi, Johnson, et al., 2015), we observe obvious shallow creep signals along the southern section of the Hayward fault. Nontectonic signals are mostly seen to the northeast of the image, possibly due to a horizontal component associated with land subsidence along the margins of the Central Valley.

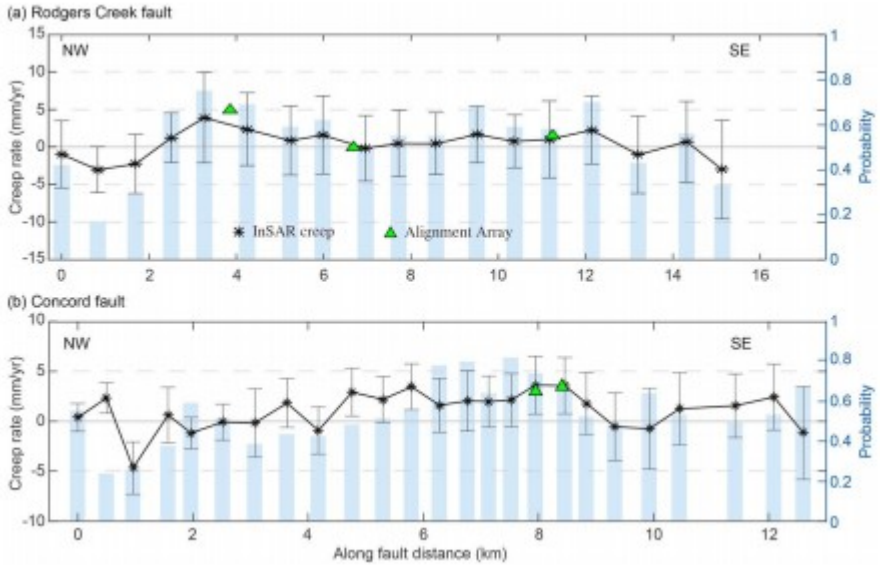

Figure 7

Along fault variations of creep rates for (a) RCF and (b) CF. The black cross represents the calculated InSAR creep rate with 68% (1σ) uncertainties. The green triangles show local creep-rate estimates from alignment arrays (Lienkaemper et al., 2014). The location of the profiles is shown in Figure 6c and

6d. Positive values reflect right-lateral creep. The shaded blue bars show the one-tailed probability of the right-lateral creep rate greater than zero (Jin & Funning, 2017).

4 Vertical Deformation in the North Bay

The InSAR vertical displacement field shows significant localized vertical motions due to geothermal, hydrological, and sediment compaction processes (Figure 8). The maximum vertical land subsidence rate of ~17 mm/year is observed in the Geysers Geothermal Field between 1992 and 2010, which is mainly associated with geothermal production (Figure 8b). This value is lower than previous subsidence estimates of up to 48 mm/year from 1994 to 1996 campaign GPS observations (Mossop & Segall, 1997), an average of 20 mm/year observed from campaign GPS measurements from 1994 and 2011 made by Floyd and Funning (2013), and an estimate of up to 50 mm/year in LOS from 1992–1999 ERS 1/2 InSAR data (Vasco et al., 2013), suggesting strong temporal variations in subsidence rates due to changing production and water injection rates. Significant localized horizontal deformation is also observed near the Geysers and appears bounded by the Collayomi fault to the east and the Maacama fault to the west (Figure 8). Other areas of significant vertical deformation are mostly localized and associated with human activities in three regions in the North Bay (Figure 8). Localized subsidence signals of up to ~7 mm/year near Rohnert Park (Figure 8c) and up to ~6 mm/year in the Sonoma Valley (Figure 8d) are related to groundwater withdrawal in local aquifers (e.g., Funning et al., 2007; Jin & Funning, 2017; McPhee et al., 2007). Differences in vertical rates in these areas between the 1992–2002 and 2006–2010 observation periods (Figure S6) are likely due to variable climate and/or groundwater withdrawal (e.g., Chaussard et al., 2014). Many regions along the western Bay margin show significant localized subsidence signals of up to 10 mm/year, likely due to consolidation of man-made fill and bay mud (e.g., Ferretti et al., 2004; Shirzaei & Bürgmann, 2018).

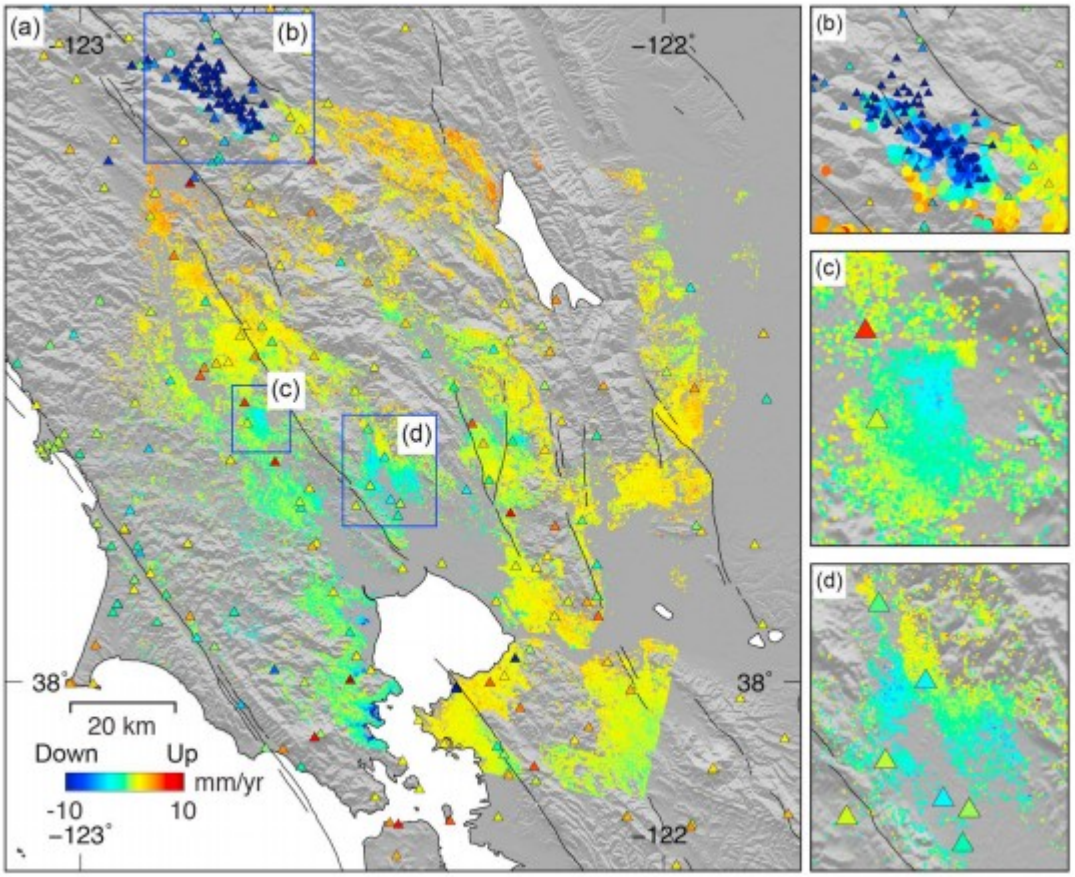

Figure 8

(a) InSAR and GPS vertical velocity field. Negative deformation rates indicate subsidence. Localized subsidence features are seen in (b) the Geysers geothermal region, (c) Rohnert Park, and (d) the Sonoma basins.

5 Discussion

Paleoseismologic studies suggest that the Rodgers Creek fault is slipping at a rate of 6.4–10.4 mm/year with a rupture recurrence interval of 131–370 year south of Santa Rosa (Budding et al., 1991; Hecker et al., 2005). Recent analyses of InSAR data suggest that the surface creeping rate of the Rodgers Creek fault is at lower rates ranging from 1.9 to 6.7 mm/year north of Santa Rosa (Funning et al., 2007; Jin & Funning, 2017). Our InSAR mean velocity field and GPS data show that a shallow aseismic creep rate of ~2 mm/year occurs in the city of Santa Rosa above a strong asperity that was inferred by Hecker et al. (2016) from gravity and magnetic field anomalies. Because of vegetation in the regions north of Santa Rosa, the ability of InSAR to resolve creep on the fault decreases significantly. We therefore do not have quantitative estimates of how much of the estimated slip deficit is accommodated by aseismic creep, and we cannot provide evidences for presence or absence of creep along the northernmost section of the Rodgers Creek fault. However, the few identified CREs along the Rodgers Creek fault

suggest that the creep rate increases from ~4 mm/year south of Santa Rosa to ~6 mm/year north of Santa Rosa.

Our results show that the predominantly right-lateral strike-slip Concord fault exhibits fault creep for much of its length. The rate increases from 2 to 4 mm/year from north to south. It is thought that the Concord fault connects with the Green Valley fault zone to the north, and the combined Concord-Green Valley fault zone has the capability to produce an event as large as M7 (Rowshandel et al., 2006), which poses significant hazards to the nearly 1 million people in Contra Costa county, as well as to the rest of the Bay Area. Trenching of the Concord fault near Galindo Creek by Borchardt et al. (1999) suggests slip rates from 3.4 to 5.4 mm/year, where 3.4 ± 0.3 mm/year was the best constrained number and 5.4 mm/year was the maximum limit. These rates are all slower than the 6.8 ± 1.4 mm/year determined geodetically from 1995 to 2005 GPS data (d'Alessio et al., 2005). The lower geologic rate is similar to the secular creep rates of 2.9–3.7 mm/year as measured by two AAs on the central Concord fault (Lienkaemper et al., 2014; McFarland et al., 2016) and our InSAR results. This would suggest that creep is accommodating nearly all motion on the fault and that large earthquakes would not be generated. There is also a possibility of temporal change in strain accumulation through shallow fault creeping. However, if the current strain accumulation rate is more similar to the geodetic rate estimated by d'Alessio et al. (2005), then only half of the Concord fault's slip budget can be explained by creep. The estimated deep slip rate (15.9 mm/year) of the Concord fault is nearly 4 times higher than the geological rate (4.3 mm/year; Field et al., 2015). We believe that this high rate likely reflects the difficulty of obtaining a slip rate on this fault from geodetic data and the shallow slip deficit rate on this fault is likely to be small.

We do not see clear surface creeping signals on the West Napa fault and other major faults in our study area. These major faults lie near urban cities including Santa Rosa, Napa, Vallejo, and Concord posing significant seismic hazards to life and property. The slip behavior of the West Napa fault is poorly constrained with slip rates ranging from ~0 to 6 mm/year (Field et al., 2015). AA data collected over 18-year period for the West Napa fault indicate no surface creep (Galehouse & Lienkaemper, 2003), but this fault produced the M6 earthquake that hit Napa County on 24 August 2014, followed by a period of localized aseismic afterslip (Feng et al., 2015; Floyd et al., 2016). We identified two CREs with a creep rate of 12 and 7 mm/year near the West Napa fault, which seem to indicate that fault creep may occur on this fault either at a rate unresolvable by our measurements or with variable rates. Similarly, no surface creep is observed geodetically for the Green Valley fault. However, AA data indicate greater creep rates on the Green Valley fault than on the Concord fault (Galehouse & Lienkaemper, 2003). The high rate of 15.9 mm/year of the Concord fault likely reflects the difficulty of obtaining a slip rate on this fault from geodetic data.

6 Conclusions

We show that time series analysis of two decades of InSAR data can be used to constrain rates of interseismic strain accumulation along major faults and resolve vertical motions in local regions in the North Bay. The decomposed InSAR horizontal mean velocity maps show evidence of shallow fault creep associated with the Rodgers Creek and Concord faults. The along-fault creep rate is ~2 mm/year on the Rodgers Creek fault near the city of Santa Rosa and up to 4 mm/year on the Concord fault, respectively. We do not observe obvious creeping signals on other major faults in the North Bay. The geodetic measurements also put constraints on the amount and patterns of vertical motion. In the Geysers geothermal region, the average land subsidence rate during the 1992–2010 period is about 10 mm/year. In the Sonoma Valley and near Rohnert Park, vertical motions at rates of >5 mm/year are most likely related to changes in groundwater level. Although the archived ERS-1/2 and Envisat InSAR data help refine the crustal deformation field of the area and resolve smaller-scale deformation features, such as aseismic fault creep, land subsidence, and geothermal deformation, the noise in the North Bay measurements still does not allow for using these data to invert for detailed coupling models on these faults, as was done for the Hayward – Calaveras faults (e.g., Chaussard, Bürgmann, Fattahi, Nadeau, et al., 2015; Schmidt et al., 2005; Shirzaei & Bürgmann, 2013). Continued acquisitions by the active Sentinel-1A/B satellites, which routinely collect data at 12-day intervals, and the L-band ALOS-2 satellite and the NASA-ISRO SAR mission should provide much improved data constraints within a few years.

Acknowledgments

We thank John Langbein, Johanna Nevitt, and two anonymous reviewers for their comments and suggestions. The ERS and Envisat original data are copyrighted by the European Space Agency and were provided through the WInSAR archive. Waveform data, metadata, and data products for this study were accessed through the Northern California Earthquake Data Center (NCEDC, 2014). The GPS velocities were provided by USGS (doi:10.5066/F7NG4NRK), UNAVCO (doi: 10.7283/T5MW2F2D). The North Bay campaign GPS velocities can be obtained from Mike Floyd (http://web.mit.edu/mfloyd/www/). Several figures were prepared by using Generic Mapping Tools software. The research was supported by a U.S. Geological Survey National Earthquake Hazards Reduction Program (NEHRP) grant (G16AP00007), the Hong Kong Polytechnic University startup grant (1-ZE6R), and the Hong Kong Research Grants Council Early Career Scheme Fund (project F-PP4B).

References

Agram, P. S., & Simons, M. (2015). A noise model for InSAR time series. *Journal of Geophysical Research: Solid Earth*, 120, 2752– 2771. https://doi.org/10.1002/2014JB011271

Beeler, N. M., Lockner, D. L., & Hickman, S. H. (2001). A simple stick-slip and creep-slip model for repeating earthquakes and its implication for

microearthquakes at Parkfield. *Bulletin of the Seismological Society of America*, 91, 1797– 1804.

Borchardt, G., D. L. Snyder, C. J. Wills (1999), Holocene slip rate of the Concord fault at Galindo Creek in Concord, California, final technical report, contract 1434-HQ-97-GR-03102, 30 pp., U.S. Geol. Surv., Menlo Park, CAL.

Budding, K. E., Schwartz, D. P., & Oppenheimer, D. H. (1991). Slip rate, earthquake recurrence, and seismogenic potential of the Rodgers Creek Fault Zone, northern California: Initial results. *Geophysical Research Letters*, 18, 447– 450. https://doi.org/10.1029/91GL00465

Bürgmann, R., Hilley, G., Ferretti, A., & Novali, F. (2006). Resolving vertical tectonics in the San Francisco Bay Area from permanent scatterer InSAR and GPS analysis. *Geology*, 34(3), 221. https://doi.org/10.1130/G22064.1

Bürgmann, R., Schmidt, D., Nadeau, R. M., d'Alessio, M., Fielding, E., Manaker, D., et al. (2000). Earthquake potential along the northern Hayward fault, California. *Science*, 289(5482), 1178– 1182.

Çakir, Z., Akoglu, A., Belabbes, S., Ergintav, S., & Meghraoui, M. (2005). Creeping along the ismetpasa section of the North Anatolian fault (western Turkey): Rate and extent from InSAR. *Earth and Planetary Science Letters*, 238(1–2), 225– 234. https://doi.org/10.1016/j.epsl.2005.06.044

Chaussard, E., Bürgmann, R., Fattahi, H., Johnson, C. W., Nadeau, R., Taira, T., & Johanson, I. (2015). Interseismic coupling and refined earthquake potential on the Hayward-Calaveras fault zone. *Journal of Geophysical Research: Solid Earth*, 120, 8570– 8590. https://doi.org/10.1002/2015JB012230

Chaussard, E., Bürgmann, R., Fattahi, H., Nadeau, R. M., Taira, T., Johnson, C. W., & Johanson, I. (2015). Potential for larger earthquakes in the East San Francisco Bay Area due to the direct connection between the Hayward and Calaveras faults. *Geophysical Research Letters*, 42, 2734– 2741. https://doi.org/10.1002/2015GL063575

Chaussard, E., Bürgmann, R., Shirzaei, M., Fielding, E. J., & Baker, B. (2014). Predictability of hydraulic head changes and characterization of aquifer-system and fault properties from InSAR-derived ground deformation. *Journal of Geophysical Research: Solid Earth*, 119, 6572– 6590. https://doi.org/10.1002/2014JB011266

d'Alessio, M. A., Johanson, I. A., Bürgmann, R., Schmidt, D. A., & Murray, M. H. (2005). Slicing up the San Francisco Bay Area: Block kinematics and fault slip rates from GPS-derived surface velocities. *Journal of Geophysical Research*, 110, B06403. https://doi.org/10.1029/2004JB003496

De Zan, F., Zonno, M., & López-Dekker, P. (2015). Phase inconsistencies and multiple scattering in SAR interferometry. *IEEE Transactions on Geoscience and Remote Sensing*, 53(12), 6608– 6616. https://doi.org/10.1109/TGRS.2015.2444431

Earthquake Engineering Research Institute (2015), M 6.0 South Napa earthquake of August 24, 2014, EERI Special Earthquake Report, California Earthquake Clearinghouse. [Available at http://www.eqclearinghouse.org/2014-08-24-south-napa/preliminary-reports/#eerireport]

Farr, T. G., Rosen, P. A., Caro, E., Crippen, R., Duren, R., Hensley, S., et al. (2007). The Shuttle Radar Topography Mission. *Reviews of Geophysics*, 45, RG2004. https://doi.org/10.1029/2005RG000183

Fattahi, H., & Amelung, F. (2016). InSAR observations of strain accumulation and fault creep along the Chaman fault system, Pakistan and Afghanistan. *Geophysical Research Letters*, 43, 8399– 8406. https://doi.org/10.1002/2016GL070121

Feng, G., Li, Z., Shan, X., Xu, B., & Du, Y. (2015). Source parameters of the 2014 Mw6.1 South Napa earthquake estimated from the Sentinel 1A, COSMO-SkyMed and GPS data. *Tectonophysics*, 655, 139– 146.

Ferretti, A., Prati, C., & Rocca, F. (2001). Permanent scatterers in SAR interferometry. *IEEE Transactions on Geoscience and Remote Sensing*, 39(1), 8– 20. https://doi.org/10.1109/36.898661

Ferretti, A., Fumagalli, A., Novali, F., Prati, C., Rocca, F., & Rucci, A. (2011). A new algorithm for processing interferometric data-stacks: SqueeSAR. *IEEE Transactions on Geoscience and Remote Sensing*, 49(9), 3460– 3470. https://doi.org/10.1109/TGRS.2011.2124465

Ferretti, A., Novali, F., Bürgmann, R., Hilley, G., & Prati, C. (2004). InSAR permanent scatterer analysis reveals ups and downs in San Francisco Bay Area. *Eos, Transactions American Geophysical Union*, 85(34), 317– 324. https://doi.org/10.1029/2004EO340002

Fialko, Y., Simons, M., & Agnew, D. (2001). The complete (3-D) surface displacement field in the epicentral area of the 1999 Mw7.1 Hector Mine earthquake, California, from space geodetic observations. *Geophysical Research Letters*, 28, 3063– 3066. https://doi.org/10.1029/2001GL013174

Field, E. H., Biasi, G. P., Bird, P., Dawson, T. E., Felzer, K. R., Jackson, D. D., et al. (2015). Long-term time-dependent probabilities for the Third Uniform California Earthquake Rupture Forecast (UCERF3). *Bulletin of the Seismological Society of America*, 105(2A), 511– 543. https://doi.org/10.1785/0120140093

Floyd, M. A., & Funning, G. J. (2013). Continuation of survey GPS measurements and installation of continuous GPS sites at The Geysers, California, for geothermal deformation monitoring. *Geothermal Resources Council Trans.*, 37, 895– 898.

Floyd, M. A., Walters, R. J., Elliott, J. R., Funning, G. J., Svarc, J. L., Murray, J. R., et al. (2016). Spatial variations in fault friction related to lithology from rupture and afterslip of the 2014 South Napa, California, earthquake.

Geophysical Research Letters, 43, 6808– 6816. https://doi.org/10.1002/2016GL069428

Fornaro, G., Pauciullo, A., & Reale, D. (2011). A null-space method for the phase unwrapping of multitemporal SAR interferometric stacks. *IEEE Transactions on Geoscience and Remote Sensing*, 49(6), 2323– 2334. https://doi.org/10.1109/TGRS.2010.2102767

Freymueller, J. T., Murray, M. H., Segall, P., & Castillo, D. (1999). Kinematics of the Pacific-North America Plate Boundary Zone, northern California. *Journal of Geophysical Research*, 104, 7419– 7441. https://doi.org/10.1029/1998JB900118

Funning, G. J., Bürgmann, R., Ferretti, A., Novali, F., & Fumagalli, A. (2007). Creep on the Rodgers Creek fault, northern San Francisco Bay area, from a 10-year PS-InSAR dataset. *Geophysical Research Letters*, 34, L19306. https://doi.org/10.1029/2007GL030836

Galehouse, J. S., & Lienkaemper, J. J. (2003). Inferences drawn from two decades of alinement array measurements of creep on faults in the San Francisco Bay region. *Bulletin of the Seismological Society of America*, 93(6), 2415– 2433. https://doi.org/10.1785/0120020226

Hanssen, R. F. (2001). *Radar interferometry: Data interpretation and error analysis*. Springer Science and Business Media, Netherlands. https://doi.org/10.1007/0-306-47633-9

Hecker, S., Langenheim, V. E., Williams, R. A., Hitchcock, C. S., & DeLong, S. B. (2016). Detailed mapping and rupture implications of the 1 km releasing bend in the Rodgers Creek fault at Santa Rosa, northern California. *Bulletin of the Seismological Society of America*, 106(2), 575– 594. https://doi.org/10.1785/0120150152

Hecker, S., Pantosti, D., Schwartz, D. P., Hamilton, J. C., Reidy, L. M., & Powers, T. J. (2005). The most recent large earthquake on the Rodgers Creek fault, San Francisco Bay Area. *Bulletin of the Seismological Society of America*, 95(3), 844– 860. https://doi.org/10.1785/0120040134

Herring, T. A. (2003). MATLAB tools for viewing GPS velocities and time series. *GPS Solutions*, 7(3), 194– 199. https://doi.org/10.1007/s10291-003-0068-0

Herring, T. A., King, R. W., & McClusky, S. C. (2010a). *GAMIT reference manual. Release 10.4*. Cambridge: Mass. Inst. Of Technol.

Herring, T. A., King, R. W., & McClusky, S. C. (2010b). *GLOBK reference manual. Release 10.4*. Cambridge: Mass. Inst. Of Technol.

Jin, L., & Funning, G. J. (2017). Testing the inference of creep on the northern Rodgers Creek fault, California, using ascending and descending persistent scatterer InSAR data. *Journal of Geophysical Research: Solid Earth*, 122, 2373– 2389. https://doi.org/10.1002/2016JB013535

Jolivet, R., Lasserre, C., Doin, M.-P., Guillaso, S., Peltzer, G., Dailu, R., et al. (2012). Shallow creep on the Haiyuan fault (Gansu, China) revealed by SAR interferometry. *Journal of Geophysical Research*, 117, B06401. https://doi.org/10.1029/2011JB008732

Lienkaemper, J. J., McFarland, F. S., Simpson, R. W., & Caskey, S. J. (2014). Using surface creep rate to infer fraction locked for sections of the San Andreas fault system in Northern California from alignment array and GPS data. *Bulletin of the Seismological Society of America*, 104(6), 3094– 3114. https://doi.org/10.1785/0120140117

Lin, Y. N., Simons, M., Hetland, E. A., Muse, P., & DiCaprio, C. (2010). A multiscale approach to estimating topographically correlated propagation delays in radar interferograms. *Geochemistry, Geophysics, Geosystems*, 11, Q09002. https://doi.org/10.1029/2010GC003228

Marinkovic, P., & Larsen, Y. (2013), Consequences of long-term ASAR local oscillator frequency decay—An empirical study of 10 years of data, Proceedings of the Living Planet Symposium, European Space Agency, Edinburgh, U. K.

McFarland, F. S., Lienkaemper, J. J., & Caskey, S. J., (2016), Data from theodolite measurements of creep rates on San Francisco Bay region faults, California, U.S. Geol. Surv. Open File Rep., 2009–1119, Menlo Park, CAL

McPhee, D. K., Langenheim, V. E., & Jachens, R. C. (2007). Basin structure beneath the Santa Rosa Plain, northern California: Implications for damage caused by the 1969 Santa Rosa and 1906 San Francisco earthquakes. *Bulletin of the Seismological Society of America*, 97(5), 1449– 1457. https://doi.org/10.1785/0120060269

Metzger, S., & Jónsson, S. (2014). Plate boundary deformation in North Iceland during the 1992-2009 revealed by InSAR time-series analysis and GPS. *Tectonophysics*, 634, 127– 138. https://doi.org/10.1016/j.tecto.2014.07.027

Monti-Guarnieri, A., & Tebaldini, S. (2008). On the exploitation of target statistics for SAR interferometry applications. *IEEE Transactions on Geoscience and Remote Sensing*, 46(11), 3436– 3443. https://doi.org/10.1109/TGRS.2008.2001756

Mossop, A., & Segall, P. (1997). Subsidence at The Geysers Geothermal Field, N. California from a comparison of GPS and leveling surveys. *Geophysical Research Letters*, 24, 1839– 1842. https://doi.org/10.1029/97GL51792

Murray, J. R., Minson, S. E., & Svarc, J. L. (2014). Slip rates and spatially variable creep on faults of the northern San Andreas system inferred through Bayesian inversion of Global Positioning System data. *Journal of Geophysical Research: Solid Earth*, 119, 6023– 6047. https://doi.org/10.1002/2014JB010966

Murray, J. R., & Svarc, J. (2017). Global Positioning System data collection, processing, and analysis conducted by the U.S. Geological Survey Earthquake Hazards Program. *Seismological Research Letters*, 88, 916– 925. https://doi.org/10.1785/0220160204

Nadeau, R. M., & McEvilly, T. V. (1999). Fault slip rates at depth from recurrence intervals of repeating microearthquakes. *Science*, 285(5428), 718– 721. https://doi.org/10.1126/science.285.5428.718

Nadeau, R. M., & McEvilly, T. V. (2004). Periodic pulsing of characteristic microearthquakes on the San Andreas fault. *Science*, 303(5655), 220– 222. https://doi.org/10.1126/science.1090353

NCEDC (2014), Northern California Earthquake Data Center. UC Berkeley Seismological Laboratory. Dataset, doi:https://doi.org/10.7932/NCEDC.

Niemi, T. M., & Hall, N. T. (1992). Late Holocene slip rate and recurrence of great earthquakes on the San Andreas fault in northern California. *Geology*, 20(3), 195– 198. https://doi.org/10.1130/0091-7613(1992)020<0195:LHSRAR>2.3.CO;2

Okada, Y. (1985). Surface deformation due to shear and tensile faults in a half-space. *Bulletin of the Seismological Society of America*, 75, 1135– 1154.

Pepe, A., & Lanari, R. (2006). On the extension of the minimum cost flow algorithm for phase unwrapping of multitemporal differential SAR interferograms. *IEEE Transactions on Geoscience and Remote Sensing*, 44(9), 2374– 2383. https://doi.org/10.1109/TGRS.2006.873207

Prescott, W. H., Savage, J. C., Svarc, J. L., & Manaker, D. (2001). Deformation across the Pacific-North America plate boundary near San Francisco, California. *Journal of Geophysical Research*, 106, 6673– 6682. https://doi.org/10.1029/2000JB900397

Reilinger, R., McClusky, S., Vernant, P., Lawrence, S., Ergintav, S., Cakmak, R., et al. (2006). GPS constraints on continental deformation in the Africa-Arabia-Eurasia continental collision zone and implications for the dynamics of plate interactions. *Journal of Geophysical Research*, 111, B05411. https://doi.org/10.1029/2005JB004051

Rocca, F. (2007). Modeling interferogram stacks. *IEEE Transactions on Geoscience and Remote Sensing*, 45(10), 3289– 3299. https://doi.org/10.1109/TGRS.2007.902286

Rowshandel, B., Reichle, M., Wills, C., Cao T., Petersen, M., Branum, D., Davis, J. (2006), Estimation of Future Earthquake Losses in California California Geological Survey, Menlo Park, California.

Ryder, I., & Bürgmann, R. (2008). Spatial variations in slip deficit on the central San Andreas fault from InSAR. *Geophysical Journal International*, 175(3), 837– 852. https://doi.org/10.1111/j.1365-246X.2008.03938.x

Schmidt, D. A., Bürgmann, R., Nadeau, R. M., & d'Alessio, M. (2005). Distribution of aseismic slip rate on the Hayward fault inferred from seismic and geodetic data. *Journal of Geophysical Research*, 110, B08406. https://doi.org/10.1029/2004JB003397

Shirzaei, M., & Bürgmann, R. (2013). Time-dependent model of creep on the Hayward fault from joint inversion of 18 years of InSAR and surface creep data. *Journal of Geophysical Research: Solid Earth*, 118, 1733– 1746. https://doi.org/10.1002/jgrb.50149

Shirzaei, M., & Bürgmann, R. (2018). Global climate change and local land subsidence exacerbate inundation risk to the San Francisco Bay Area. *Science Advances*, 4. eaap9234. https://doi.org/10.1126/sciadv.aap9234

Thatcher, W., Marshall, G., & Lisowski, M. (1997). Resolution of fault slip along the 470-km-long rupture of the great 1906 San Francisco earthquake and its implications. *Journal of Geophysical Research*, 102, 5353– 5367. https://doi.org/10.1029/96JB03486

Tong, X., Sandwell, D. T., & Smith-Konter, B. (2013). High-resolution interseismic velocity data along the San Andreas fault from GPS and InSAR. *Journal of Geophysical Research: Solid Earth*, 118, 369– 389. https://doi.org/10.1029/2012JB009442

Turner, R. C., Nadeau, R. M., & Bürgmann, R. (2013). Aseismic slip and fault interaction from repeating earthquakes in the Loma Prieta aftershock zone. *Geophysical Research Letters*, 40, 1079– 1083. https://doi.org/10.1002/grl.50212

Vasco, D. W., Rutqvist, J., Ferretti, A., Rucci, A., Bellotti, F., Dobson, P., et al. (2013). Monitoring deformation at The Geysers Geothermal Field, California using C-band and X-band interferometric synthetic aperture radar. *Geophysical Research Letters*, 40, 2567– 2572. https://doi.org/10.1002/grl.50314

Wong, I. G., & Bott, J. D. J. (1995). A new look back at the 1969 Santa Rosa, California, earthquakes. *Bulletin of the Seismological Society of America*, 85(1), 334– 341.

Wright, T., Parsons, B., & Fielding, E. (2001). Measurement of interseismic strain accumulation across the North Anatolian Fault by satellite radar interferometry. *Geophysical Research Letters*, 28, 2117– 2120. https://doi.org/10.1029/2000GL012850

Zhang, J., Bock, Y., Johnson, H., Fang, P., Williams, S., Genrich, J., et al. (1997). Southern California Permanent GPS Geodetic Array: Error analysis of daily position estimates and site velocities. *Journal of Geophysical Research*, 102, 18,057– 18,070. https://doi.org/10.1029/97JB01378

Zhang, L., Ding, X., & Lu, Z. (2011). Modeling PSInSAR time series without phase unwrapping. *IEEE Transactions on Geoscience and Remote Sensing*, 49(1), 547– 556. https://doi.org/10.1109/TGRS.2010.2052625